








The Triple-layered Leading Edge of Solar Coronal Mass Ejections

Z. X. Mei^{1,2} , R. Keppens³ , Q. W. Cai⁴ , J. Ye^{1,2} , Y. Li^{1,2}, X. Y. Xie^{1,2,5,6}, and J. Lin^{1,2,5} 

¹ Yunnan Observatories, Chinese Academy of Sciences, Kunming, Yunnan 650011, People's Republic of China

² Center for Astronomical Mega-Science, Chinese Academy of Sciences, Beijing 100101, People's Republic of China

³ Centre for mathematical Plasma Astrophysics, Department of Mathematics, KU Leuven, Celestijnenlaan 200B, 3001 Leuven, Belgium

⁴ Institute of Space Physics, Luoyang Normal University, Luoyang, People's Republic of China

⁵ University of Chinese Academy of Sciences, 19A Yuquan Road, Beijing 100049, People's Republic of China

⁶ Harvard-Smithsonian Center for Astrophysics, 60 Garden Street, Cambridge, MA 02138, USA

Received 2020 May 11; revised 2020 July 2; accepted 2020 July 3; published 2020 July 22

Abstract

In a high-resolution, 3D resistive magnetohydrodynamic simulation of an eruptive magnetic flux rope (MFR), we revisit the detailed 3D magnetic structure of a coronal mass ejection (CME). Our results highlight that there exists a helical current ribbon/boundary (HCB) that wraps around the CME bubble. This HCB results from the interaction between the CME bubble and the ambient magnetic field, where it represents a tangential discontinuity in the magnetic topology. Its helical shape is ultimately caused by the kinking of the MFR that resides within the CME bubble. In synthetic Solar Dynamics Observatory/Atmospheric Imaging Assembly images, processed to logarithmic scale to enhance otherwise unobservable features, we show a clear triple-layered leading edge: a bright fast shock front, followed by a bright HCB, and within it a bright MFR. These are arranged in sequence and expand outward continuously. For kink unstable eruptions, we suggest that the HCB is a possible explanation for the bright leading edges seen near CME bubbles and also for the non-wave component of global EUV disturbances.

Unified Astronomy Thesaurus concepts: [Solar coronal mass ejections \(1997\)](#); [Solar coronal waves \(1995\)](#); [Solar magnetic fields \(1503\)](#); [Magnetohydrodynamical simulations \(1966\)](#); [Magnetohydrodynamics \(1964\)](#); [Solar filament eruptions \(1981\)](#); [Solar prominences \(1519\)](#); [Solar extreme ultraviolet emission \(1493\)](#)

1. Introduction

Coronal mass ejections (CMEs) usually result from rapidly erupting magnetic flux ropes (MFRs). These MFRs may exist prior to the eruption, containing filaments/prominences (Lin & Forbes 2000; Gopalswamy et al. 2003; Yan et al. 2012) or hot channels (Cheng et al. 2014; Cheng & Ding 2016), or form during the CME eruption (Mikic & Linker 1994; Antiochos et al. 1999). In the past two solar cycles, observations using white-light coronagraphs demonstrated that 30% of CMEs have three components, a bright leading front enclosing a dark cavity, which contains a bright core (Webb & Howard 2012). Recently, such three-part components have also been observed in the early stages of eruptions (in the low corona) in extreme-ultraviolet (EUV) passbands (Song et al. 2017, 2019).

It still remains an open question as to how these erupting MFRs evolve into the typical CMEs with three components (Manchester et al. 2017). The CME cores used to be interpreted as eruptive filaments (Gilbert et al. 2000). However, Howard et al. (2017) performed a statistical work based on looking into 42 CMEs with three-part structures and illustrated that 70% of the events are not associated with filaments. Theories for the CME front/leading edges are fairly involved and reviewed in Chen (2011) and Warmuth (2015). Early theory regarded the CME front as a fast-mode magnetohydrodynamic (MHD) wave (Nakagawa et al. 1975), but this was discarded since the legs of the CME front do not expand laterally at several solar radii in observations (Howard et al. 1982). Later, the CME front was interpreted as coronal plasma pileup in front of the eruptive MFR (Forbes et al. 2006; Thernisien et al. 2009). However, the physical mechanism of this plasma pileup needs further investigation. A third interpretation involves a bimodal (wave and non-wave) aspect of coronal EUV waves, in which the

non-wave components of EUV disturbances relate to the expanding CME leading edges (Chen et al. 2002).

Numerical experiments have been performed extensively to study the eruption process of CMEs, including their triggering mechanism (Forbes 1990), the reconnecting current sheet (CS; Reeves et al. 2019), the large-scale evolution (Roussev et al. 2012; Jiang et al. 2018), and the associated coronal EUV disturbances (Delannée et al. 2008; Downs et al. 2012). In earlier numerical studies preceding modern CME simulations, evolutions of cylindrical straight MFRs have been simulated as well (Baty 2001; Bareford et al. 2010). These all demonstrate that, usually, a current concentration wraps around the straight MFR and takes the form of a helical current ribbon/boundary (HCB) during the nonlinear development of the kink instability. Its formation is due to the interaction between the MFR and the ambient magnetic field. Török et al. (2004) and Mei et al. (2018) studied the kink instability in torus-shaped MFRs, and also confirmed the formation of this HCB surrounding the MFR, where the eruptive magnetic structure collides with the overlying background.

Here, we perform a high-resolution 3D resistive MHD simulation on the basis of the Titov & Démoulin (1999) model (TD99; also in Lin et al. 2002), and we employ forward modeling (van Doorselaere et al. 2016) to obtain synthetic Solar Dynamics Observatory (SDO)/Atmospheric Imaging Assembly (AIA) images, which allows a direct comparison with observations. Our goal is to highlight the magnetic and overall structure of the CME and its interaction with the background field as it departs from the lower corona. In Section 2, the setup of this numerical experiment is given. In Section 3, the results are presented, and Section 4 summarizes our work.

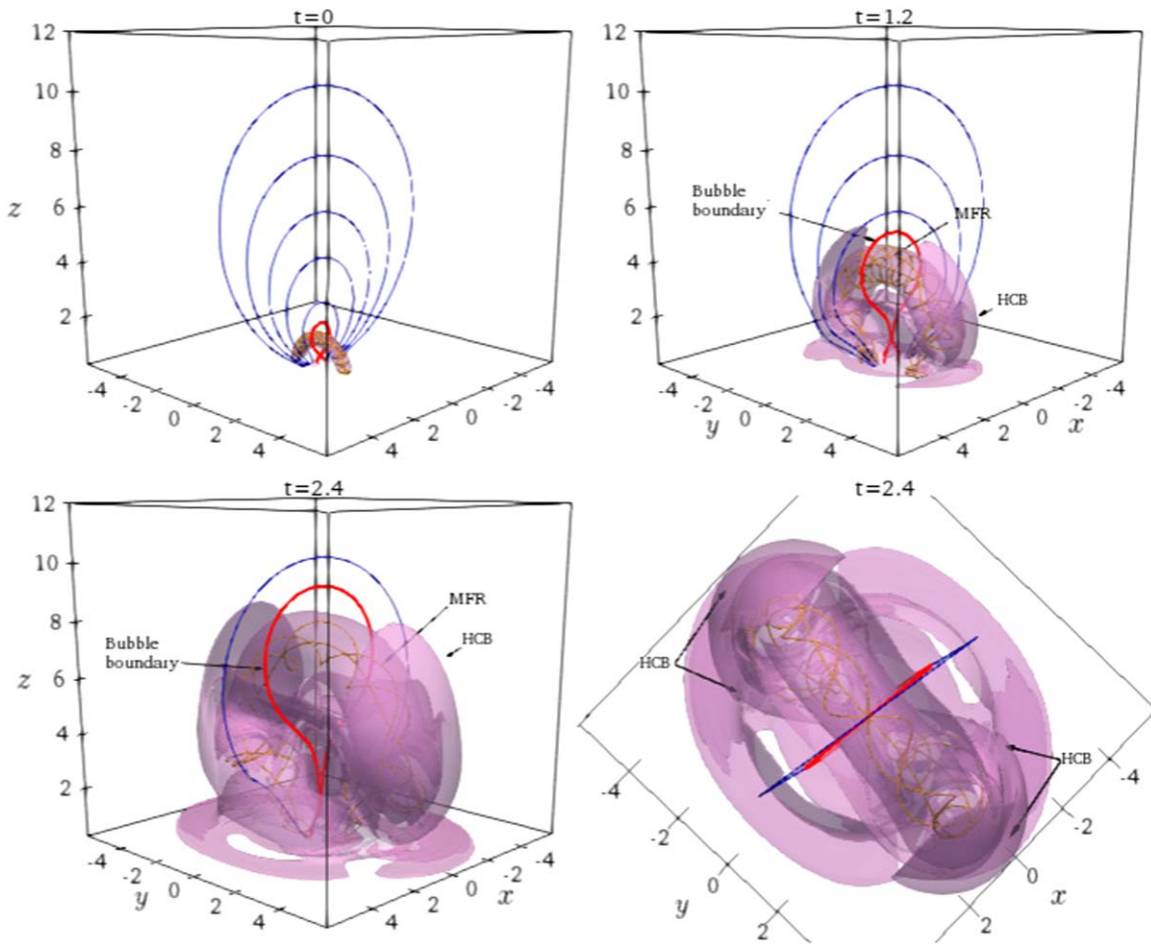


Figure 1. Evolution snapshots of magnetic structure during the eruption. The dimensionless units of time and length are 4.293×10^2 s and 5×10^9 cm, respectively. Colorful curves are magnetic field lines of the background field (blue) and the field inside the MFR (golden). Red curve is the CME bubble boundary. The pink surfaces are current isosurfaces with different values 10, 1.5, and 0.4, respectively. Text marked on figure are the CME bubble boundary, the HCB, and the MFR.

2. Setup of Numerical Simulation

The initial magnetic configuration comes from the TD99 model, which consists of three parts, as shown in the upper left panel of Figure 1. The first part is the MFR with major radius R , minor radius a , and total current I , uniformly distributed over its circular cross-section. The second is a background field due to a pair of magnetic sources $\pm q$ separated by a distance L , lying on the symmetry axis of the MFR, buried at $z = d$ below the photospheric surface $z = z_p$. In order to control the twist of the MFR, a third part is introduced by a dipole located at $z = d_d$ on the z -axis with strength q_d and direction along the y -axis (Mei et al. 2020).

A two-layer, gravitationally stratified atmosphere is employed. Gravity $\rho \mathbf{g}$ is along the z -axis and $\mathbf{g} = g_\odot \hat{z} / (1 + z/R_\odot)^2$ with $g_\odot = -2.742 \times 10^{-4}$ cm s $^{-1}$ being the gravity acceleration at $z = z_p$. The atmosphere with $z \leq z_p$ and $z > z_p$ represents the photosphere and the extended corona. The transition region has not been included in our simulation. The initial temperature is T_p under the photosphere and T_c above the photosphere such that we obtain a layer with high density and a sharp increase in pressure near the bottom of the simulation box. The photosphere is to provide a line-tied environment in the bottom region that includes a high-density layer such that the foot-points of magnetic field lines are anchored into the photosphere. We do not pay much attention to the physical processes below the bottom of the corona, as our treatment just serves to easily handle the line-tied bottom boundary. For all five other boundaries, we use open

boundaries: all physical variables in the ghost cells are deduced via extrapolation of internal grid points.

The resistive MHD equations in our simulation are solved by the MPI-parallelized adaptive mesh refinement code MPI-AMRVAC⁷ (Keppens et al. 2012; Porth et al. 2014; Xia et al. 2018). We employ a third-order accurate shock-capturing finite volume spatial discretization, using a Harten–Lax–van Leer approximate Riemann Solver (Harten 1983), a third-order limited reconstruction (Čada & Torrilhon 2009), and a three-step Runge–Kutta time marching method. We assume fully ionized atmosphere with the adiabatic index $\gamma = 5/3$. The heat conduction is purely field aligned and temperature dependent, hence the heat conduction $\kappa = \kappa_{\parallel} T^{2.5} \hat{e}_B \hat{e}_B$. The unit vector $\hat{e}_B = \mathbf{B}/|\mathbf{B}|$ and $\kappa_{\parallel} = 10^{-6}$ erg s $^{-1}$ cm $^{-1}$ K $^{-3.5}$. The radiative losses and the additional heat term have not been considered in our simulation.

For convenience, all physical quantities are normalized to 5×10^9 cm, 1.165×10^7 cm s $^{-1}$, 4.293×10^2 s, 2.342×10^{-14} g cm $^{-3}$, 10^6 K, 3.175 Pa, 6.317 G, and 7.54×10^{20} A for length, velocity, time, density, temperature, pressure, magnetic field, and electric current intensity, respectively. The computation domain is a 3D box of sizes $-6 \leq x \leq 6$, $-6 \leq y \leq 6$, and $0 \leq z \leq 12$ in a Cartesian coordinate system, and 360^3 grid points are uniformly distributed. The relevant

⁷ <http://amrvac.org/>

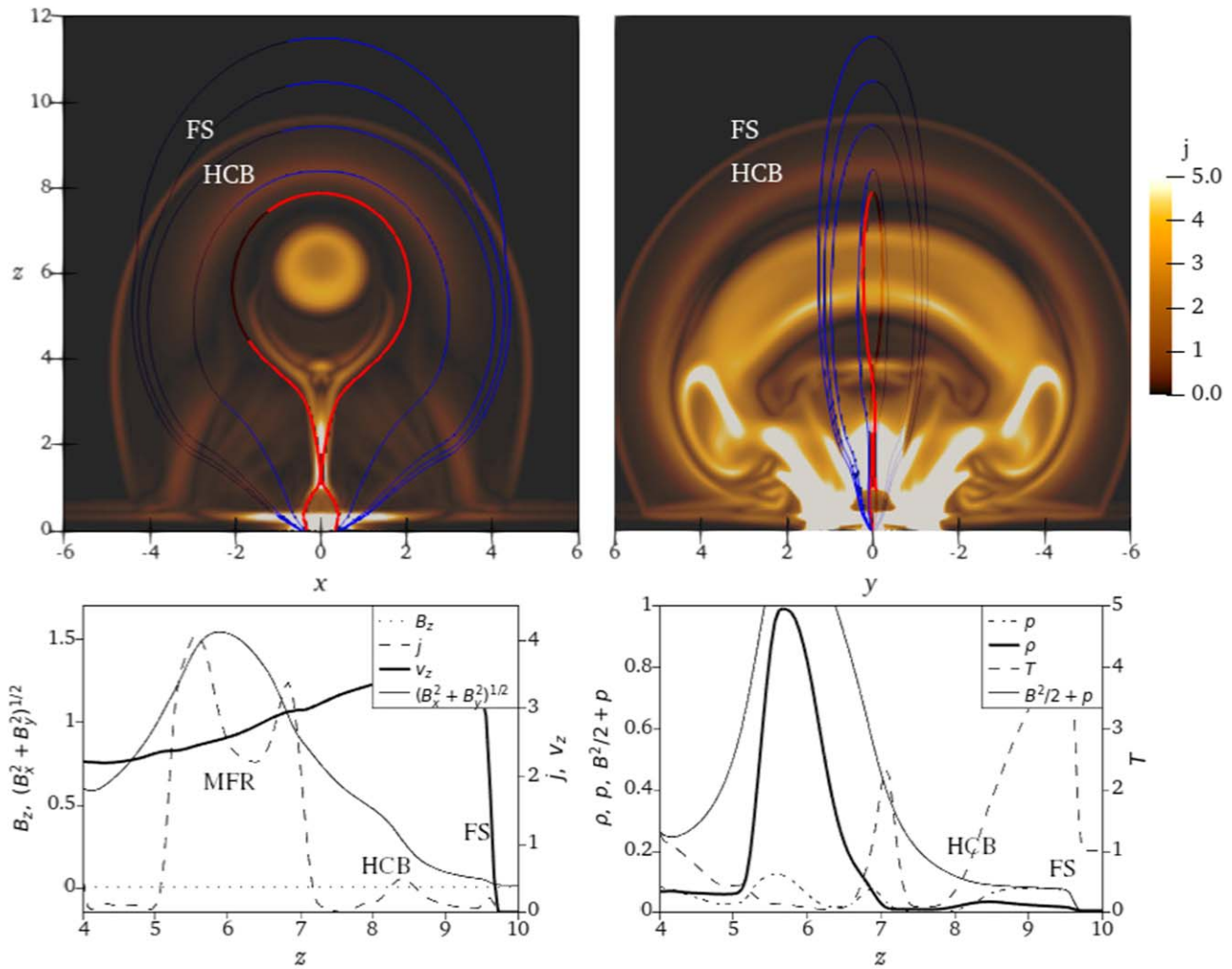


Figure 2. Upper: distributions of the current on the cuts $y = 0$ (left) and $x = 0$ (right) at $t = 2$. The colorful curves are the magnetic field lines outside the MFR (blue) and the boundary of the CME bubble (red). Marked on this figure are the MFR and the fast-mode shock (FS). Lower: distribution of different physical quantities along the z -axis.

parameters R , a , d , d_d , L , q , I , z_p , T_p , and T_c are set to 1.2, 0.2, -0.1 , -1.2 , 0.3, 22.8, 83.2, 0.4, 0.006, and 1, respectively. The uniform resistivity $\eta = 6 \times 10^{-4}$ and so the resulting Reynolds number is about 2×10^3 . In addition, the uniform temperature inside the MFR is set to $T_{\text{in}} = 0.04$, and the total mass inside the MFR equals about 95 (in our units), i.e., 4.66×10^{16} g.

3. Numerical Results

For the construction of the initial magnetic field, we first obtain an MFR in a perfect force-balanced equilibrium state, on which the upward hoop force of the MFR has been balanced by the downward force from the ambient background field. To let the MFR erupt, we intentionally decrease the strength of the background field by a factor of 0.8. Further details are described by Mei et al. (2020). Due to an intentional departure from the equilibrium and the high twist, the MFR erupts immediately after the launch of the simulation, and experiences kink instability simultaneously. Evolution snapshots of the magnetic structure are shown in Figure 1. The colored curves are magnetic field lines inside or outside the MFR. The red curve represents the outermost magnetic field line of the CME bubble, which is referred to as the “boundary” of the CME

bubble (see also the discussion of Lin et al. 2004; Lin & Soon 2004). Pink current isosurfaces show the 3D geometrical shape of current structures. During the eruption, the MFR moves upward and expands its volume significantly. Around the MFR, an HCB (marked in Figure 1) appears and also expands continuously. This HCB has been reported by many studies on kink processes of straight cylindrical MFRs (Hood et al. 2009; Gordovskyy et al. 2014; Pinto et al. 2015) and of torus-shaped MFRs (Török et al. 2004; Mei et al. 2018). For the straight case, the kinking MFR interacts with the ambient magnetic field, so that a helical CS/ribbon forms and wraps around the MFR. For torus-shaped ropes, the MFR is embedded entirely into the CME bubble, as shown by the red curves in Figure 1. Instead of the MFR field, it is the entire CME bubble that serves as an agent for the kinking MFR within it, to interact with the ambient background magnetic field.

The resultant HCB is exterior to the bubble boundary but wraps around the bubble tightly, as shown in Figure 2. Because the HCB is along the magnetic field (seen in the upper left panel of Figure 2), this HCB is a tangential discontinuity between two different magnetic systems (Priest 2014). The

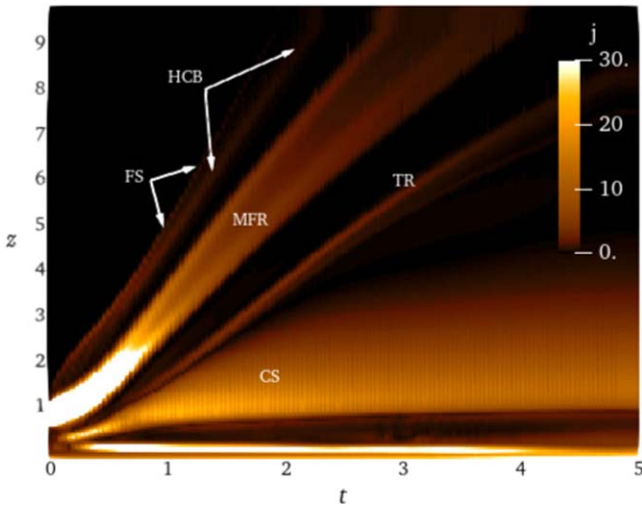


Figure 3. Spatio-temporal map for the long-strip cut $y = 0$ along the z -axis. The golden shading gives the distribution of current. Marked on figure are the FS, the HCB, the MFR, the TR, and the reconnecting CS.

lower panels of Figure 2 give the distributions of different physical quantities along the z -axis. On the distribution of the current intensity j , we can see the MFR, the HCB, and the FS clearly. The helical geometry of this HCB results from the kink process of the MFR within the bubble, which rotates the MFR during its upward eruption. In addition, it is worth mentioning that the HCB and the bubble boundary have completely different physical properties although they are fairly close in space. The bubble boundary has been defined as the outermost magnetic field line of the CME bubble, which separates the magnetic system inside the bubble from the outside.

In Figure 3, a spatio-temporal map from the long-strip cut $y = 0$ along the z -axis shows the evolution of the current distribution during the eruption. In this figure, the fast shock (FS), the HCB, the MFR, the highly nonlinear turbulence region (TR), and the reconnecting CS have been marked. Here, the TR identifies the intensive interaction between the CME bubble and the reconnection outflow from the underlying CS (Nishida et al. 2013; Takahashi et al. 2017; Ye et al. 2019). Thus, the TR indicates the lowest point of the bubble boundary and the upper tip of the CS. For the MFR, it shows a clear acceleration of 1.7 km s^{-2} in the early stage of the simulation. Later, it moves upward with a uniform speed of about 367 km s^{-1} due to the gradual decrease of its acceleration, and its cross-section radius displays an obvious expansion. In front of the MFR, the FS propagates upward with a constant speed of about 520 km s^{-1} , and the HCB expands with a speed about 470 km s^{-1} . Due to the speed difference, a gradual slow separation develops between the MFR, the FS, and the HCB. The separation between the MFR and the FS is not due to the slowing down of the MFR. The FS is driven by the MFR. It is a piston-driven shock, and its propagation speed can be much faster than its driver. Thus, the FS can separate from the MFR quickly.

To obtain the corresponding observational consequences, we performed forward modeling of SDO/AIA observables by the forward modeling code (van Doorselaere et al. 2016), which calculates the EUV emission from the optically thin coronal plasma. Two angles \mathcal{L} and $-\mathcal{B}$ connect the coordinate system x - y - z in our experiment with x' - y' - z' in the rotated frame of

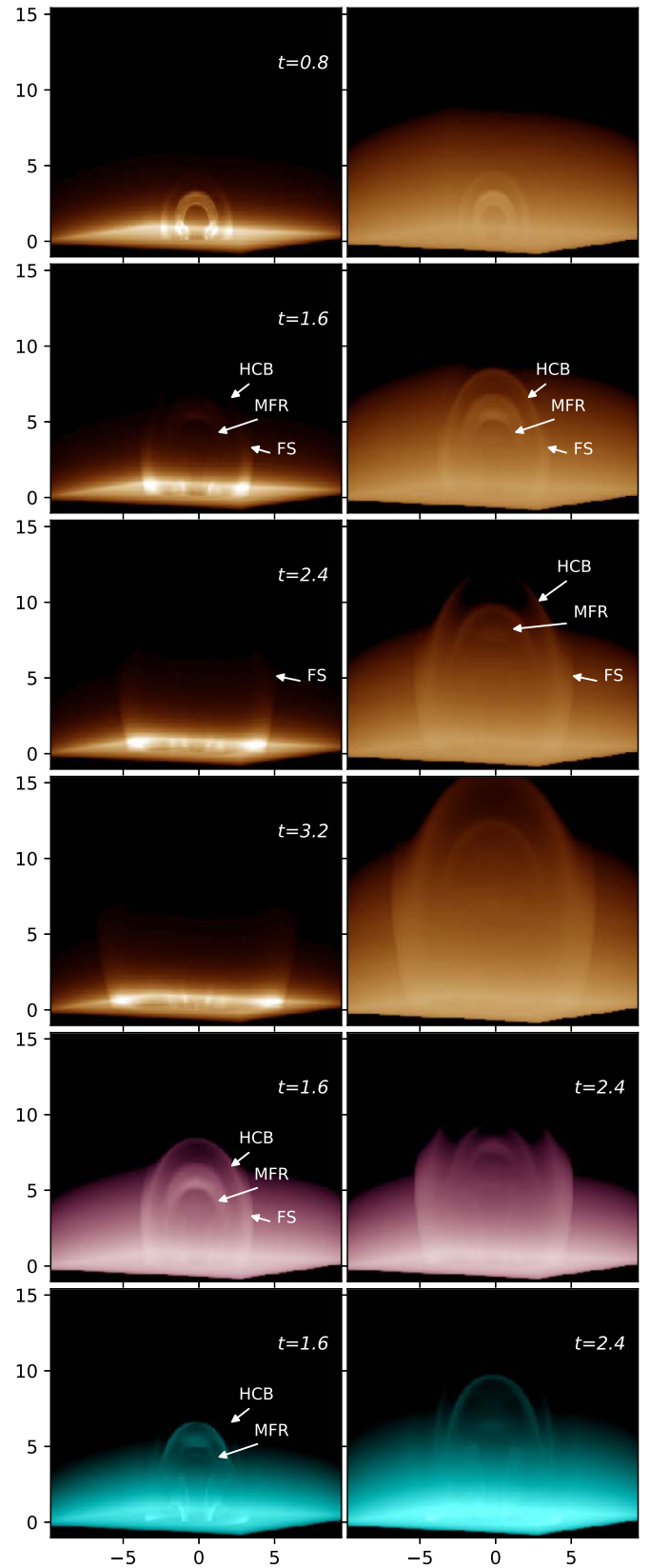


Figure 4. Left bronze: synthetic AIA 193 \AA snapshots in the image plane (i.e., the plane-of-the-sky) with viewing angles $\mathcal{L} = -30^\circ$ and $\mathcal{B} = 86^\circ$ at different times. Right bronze: same as the left column, but in a log-scale. Pink and green: synthetic AIA 211 \AA (pink) and 131 \AA (green) images in a log-scale with the same viewing angles.

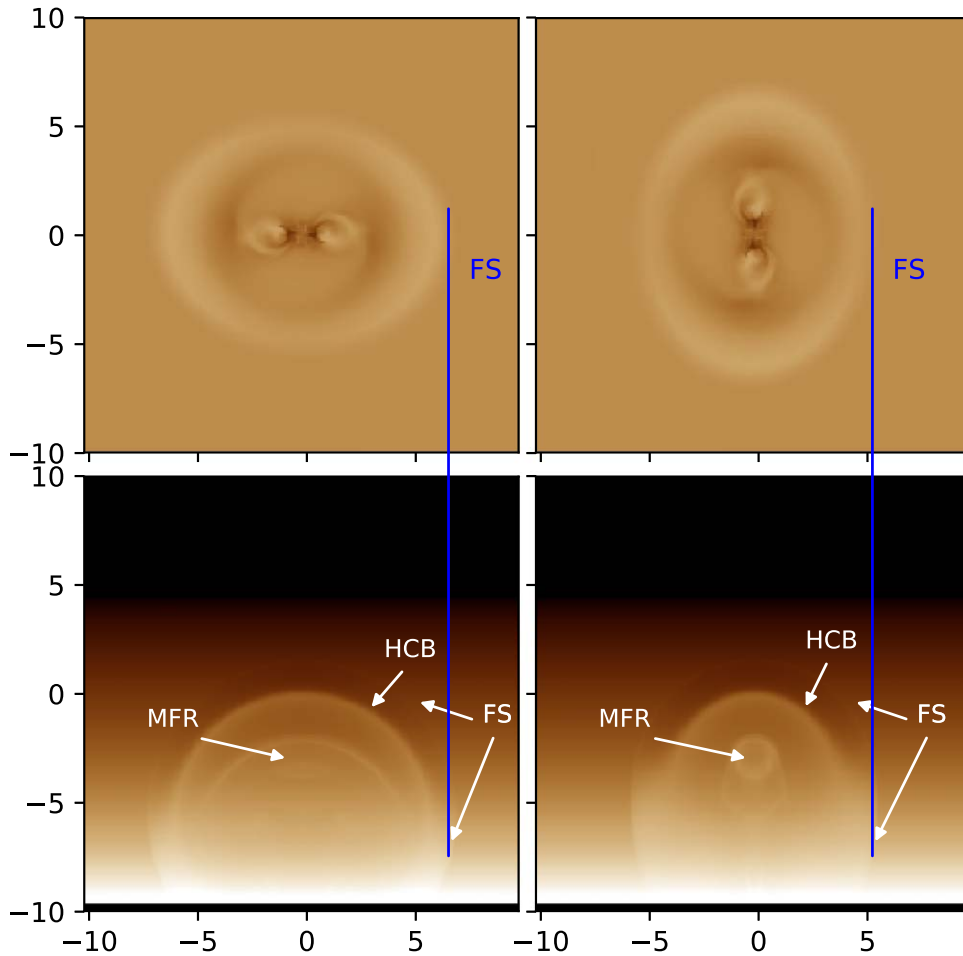


Figure 5. Synthetic AIA 193 Å images at $t = 2$ with log-scale from different viewing angles: $\mathcal{L} = 0^\circ$ and $\mathcal{B} = 0^\circ$ for the upper left panel, $\mathcal{L} = -90^\circ$ and $\mathcal{B} = 0^\circ$ for the upper right panel, $\mathcal{L} = 0^\circ$ and $\mathcal{B} = -90^\circ$ for the lower left panel, and $\mathcal{L} = -90^\circ$ and $\mathcal{B} = -90^\circ$ for the lower right panel.

reference of the observation. Here, \mathcal{L} is between the line of sight (LOS) and the z -axis, $-\mathcal{B}$ is between the LOS and the y -axis, and $x'-y'$ is the synthetic image plane (i.e., the plane-of-the-sky). Panels of Figure 4 with bronze color show synthetic images of SDO/AIA 193 Å snapshots at different times, with viewing angles $\mathcal{L} = 30^\circ$ and $-\mathcal{B} = 86^\circ$. The synthetic AIA 193 Å images in the left bronze panels of Figure 4 are the same as the images in the right bronze panels, but the latter use a log-scale to highlight otherwise hidden features.

In the original left bronze panels, we can see a 3D FS hemispherical front and a bright MFR. The 3D FS front is seen clearly in the AIA 193 Å images, because the plasma temperature and density following the FS front increase significantly. Because the untwisting process creates lots of substructures, and so speeds up the ohmic heating and the magnetic reconnection, plasma inside the MFR is heated to $T = 6$ MK in the early stages of our resistive MHD experiment, so that the dark MFR in the beginning of the simulation lights up later in the synthetic AIA images. When this heated MFR experiences continuous expansion, the increase of total MFR volume results in a dramatic decrease in its internal temperature in the subsequent evolution, so the MFR gradually darkens and disappears in the image.

In the logarithmically stretched right bronze panels of Figure 4, more features can be discovered in the synthetic images. First, the HCB can be seen clearly, situated in between the FS front and the MFR during eruption. Second, the MFR

can also be identified from the ambient background at later stages of the eruption, although it becomes invisible in the unprocessed corresponding images in the left panels. Figure 4 also displays AIA synthetic images with the log-scale in 211 and 131 Å. The HCB and the MFR can be identified easily in these bands during the whole simulation as well. The FS can be seen in AIA 211 Å, but is absent in 131 Å, because of its contribution function (Lemen et al. 2012).

In the enhanced synthetic images, the HCB, the bright MFR, and the dimming regions between them together form the typical three components of the CME. This is to say, our results here suggest that the leading edge of the CME is the HCB, which is close to, but different from the boundary of the CME bubble. According to the bimodal interpretation of global EUV disturbances, the FS front is followed by a non-wave diffusive front, which has been related to the leading edge of the CME (Chen 2011; Warmuth 2015). We here further suggest that the non-wave component corresponds to the HCB in our synthetic images. However, it is unclear that the current boundary can also form and be observed in synthetic images during the MFR eruption without involving the kink instability.

Because the EUV emission measure depends in an important way on the orientation of the LOS, synthetic AIA 193 Å images with different viewing angles are given in Figure 5. The upper panels show the EUV disturbance observed near the center of the solar disk, and the lower panels show the EUV disturbance observed at the limb. In the lower panels, the FS, the HCB, and

the MFR can be identified clearly at $t = 2$. In the upper panels, on the other hand, only a diffusive front can be identified and the FS, the HCB, and the MFR cannot be identified although all of these structures have a contribution to the EUV emission of disturbances on the solar disk. In the upper panels, the outer edge of the EUV disturbance is determined by the outermost part of the FS hemispherical front, instead of the FS front nearby the photosphere, as indicated by blue lines in Figure 5.

4. Conclusion

When the MFR erupts upward, the reconnecting CS below it grows continuously, in which magnetic field lines disconnect and reconnect to form new closed magnetic field lines, which outline the boundary of the expanding CME bubble. Wrapping around this bubble, a 3D helical current ribbon/boundary (namely HCB) develops. This HCB results from the interaction of the CME bubble with the background magnetic field. Its helical topology is indirectly caused by the kink instability of the MFR that happens in the center of the CME bubble.

We created synthetic images of SDO/AIA in different bands by employing forward modeling for EUV observations. Because of the untwisting process, the internal plasma of the MFR gets heated significantly so that it can be observed in synthetic images in the early stage of the simulation. Above the MFR, the FS dome as a 3D hemispherical front can be seen to propagate outward continuously. In the log scaling, the HCB also can be identified clearly as a bright front between the FS and the MFR in enhanced synthetic images. The HCB, the MFR, and the dimming region between them together form the typical three-component structure of a CME, which can be observed in the enhanced synthetic images during the whole eruption. The HCB in our simulation corresponds to the outermost component of the CME, i.e., the CME leading edge in observations. According to the bimodal interpretation of EUV disturbances, a non-wave component relates to the expanding of the leading edge of the CME. Here, we rather suggest that the previously underresolved HCB component may form the non-wave component of large-scale EUV disturbances.

The authors thank Caowei Jiang for fruitful discussions. This work was supported by the Strategic Priority Research Program of CAS with grants XDA17040507 and QYZDJ-SSWLSH012; the National Science Foundation of China (NSFC) under the grant Nos. 11933009, U1631130, 11273055, 11303088, 11573064, 11403100, 11333007, and 11973083; the project of the Group for Innovation of Yunnan Province grant 2018HC023; the Yunnan Ten-Thousand Talents Plan-Yunling Scholar Project; the Applied Basic Research of Yunnan Province in China grants 2019FB005 and 2018FB009; as well as a joint FWO-NSFC grant G0E9619N; and received funding from the European Research Council (ERC) under the European Unions Horizon 2020 research and innovation program (grant agreement No. 833251 PROMINENT ERC-ADG 2018), and from Internal Funds KU Leuven, project C14/19/089 TRACESpace. The work was carried out on the cluster in the Computational Solar Physics lab of Yunnan Observatories.

ORCID iDs

Z. X. Mei  <https://orcid.org/0000-0001-9650-1536>
R. Keppens  <https://orcid.org/0000-0003-3544-2733>

Q. W. Cai  <https://orcid.org/0000-0001-5188-0165>
J. Ye  <https://orcid.org/0000-0002-5983-104X>
J. Lin  <https://orcid.org/0000-0002-3326-5860>

References

- Antiochos, S. K., DeVore, C. R., & Klimchuk, J. A. 1999, *ApJ*, 510, 485
Bareford, M. R., Browning, P. K., & van der Linden, R. A. M. 2010, *A&A*, 521, A70
Baty, H. 2001, *A&A*, 367, 321
Ćada, M., & Torrilhon, M. 2009, *JCoPh*, 228, 4118
Chen, P. F. 2011, *LRSP*, 8, 1
Chen, P. F., Wu, S. T., Shibata, K., & Fang, C. 2002, *ApJL*, 572, L99
Cheng, X., & Ding, M. D. 2016, *ApJS*, 225, 16
Cheng, X., Ding, M. D., Zhang, J., et al. 2014, *ApJ*, 789, 93
Delannée, C., Török, T., Aulanier, G., & Hochedez, J. F. 2008, *SoPh*, 247, 123
Downs, C., Roussev, I. I., van der Holst, B., Lugaz, N., & Sokolov, I. V. 2012, *ApJ*, 750, 134
Forbes, T. G. 1990, *JGR*, 95, 11919
Forbes, T. G., Linker, J. A., Chen, J., et al. 2006, *SSRv*, 123, 251
Gilbert, H. R., Holzer, T. E., Burkepile, J. T., & Hundhausen, A. J. 2000, *ApJ*, 537, 503
Gopalswamy, N., Lara, A., Yashiro, S., & Howard, R. A. 2003, *ApJL*, 598, L63
Gordovskyy, M., Browning, P. K., Kontar, E. P., & Bian, N. H. 2014, *A&A*, 561, A72
Harten, A. 1983, *JCoPh*, 49, 357
Hood, A. W., Browning, P. K., & van der Linden, R. A. M. 2009, *A&A*, 506, 913
Howard, R. A., Michels, D. J., Sheeley, N. R. J., & Koomen, M. J. 1982, *ApJL*, 263, L101
Howard, T. A., DeForest, C. E., Schneck, U. G., & Alden, C. R. 2017, *ApJ*, 834, 86
Jiang, C., Zou, P., Feng, X., et al. 2018, *ApJ*, 869, 13
Keppens, R., Meliani, Z., van Marle, A. J., et al. 2012, *JCoPh*, 231, 718
Lemen, J. R., Title, A. M., Akin, D. J., et al. 2012, *SoPh*, 275, 17
Lin, J., & Forbes, T. G. 2000, *JGR*, 105, 2375
Lin, J., Raymond, J. C., & van Ballegooijen, A. A. 2004, *ApJ*, 602, 422
Lin, J., & Soon, W. 2004, *NewA*, 9, 611
Lin, J., van Ballegooijen, A. A., & Forbes, T. G. 2002, *JGRA*, 107, 1438
Manchester, W., Kilpua, E. K. J., Liu, Y. D., et al. 2017, *SSRv*, 212, 1159
Mei, Z. X., Keppens, R., Cai, Q. W., et al. 2020, *MNRAS*, 493, 4816
Mei, Z. X., Keppens, R., Roussev, I. I., & Lin, J. 2018, *A&A*, 609, A2
Mikic, Z., & Linker, J. A. 1994, *ApJ*, 430, 898
Nakagawa, Y., Wu, S. T., & Tandberg-Hanssen, E. 1975, *SoPh*, 41, 387
Nishida, K., Nishizuka, N., & Shibata, K. 2013, *ApJL*, 775, L39
Pinto, R. F., Vilmer, N., & Brun, A. S. 2015, *A&A*, 576, A37
Porth, O., Xia, C., Hendrix, T., Moschou, S. P., & Keppens, R. 2014, *ApJS*, 214, 4
Priest, E. 2014, *Magnetohydrodynamics of the Sun* (Cambridge: Cambridge Univ. Press)
Reeves, K. K., Török, T., Mikić, Z., Linker, J., & Murphy, N. A. 2019, *ApJ*, 887, 103
Roussev, I. I., Galsgaard, K., Downs, C., et al. 2012, *NatPh*, 8, 845
Song, H. Q., Cheng, X., Chen, Y., et al. 2017, *ApJ*, 848, 21
Song, H. Q., Zhang, J., Li, L. P., et al. 2019, *ApJL*, 887, 124
Takahashi, T., Qiu, J., & Shibata, K. 2017, *ApJ*, 848, 102
Thernisien, A., Vourlidas, A., & Howard, R. A. 2009, *SoPh*, 256, 111
Titov, V. S., & Démoulin, P. 1999, *A&A*, 351, 707
Török, T., Kliem, B., & Titov, V. S. 2004, *A&A*, 413, L27
van Doorselaere, T., Antolin, P., Yuan, D., Reznikova, V., & Magyar, N. 2016, *FrASS*, 3, 4
Warmuth, A. 2015, *LRSP*, 12, 3
Webb, D. F., & Howard, T. A. 2012, *LRSP*, 9, 3
Xia, C., Teunissen, J., El Mellah, I., Chané, E., & Keppens, R. 2018, *ApJS*, 234, 30
Yan, X. L., Qu, Z. Q., Kong, D. F., & Xu, C. L. 2012, *ApJ*, 754, 16
Ye, J., Shen, C., Raymond, J. C., Lin, J., & Ziegler, U. 2019, *MNRAS*, 482, 588